Interpretation of rotation and momentum transport in the DIII-D edge plasma and comparison with neoclassical theory

2014 Nucl. Fusion 54 073021

(http://iopscience.iop.org/0029-5515/54/7/073021)

IOP Publishing | International Atomic Energy Agency Nuclear Fusion
Nucl. Fusion **54** (2014) 073021 (11pp) doi:10.1088/0029-5515/54/7/073021

Interpretation of rotation and momentum transport in the DIII-D edge plasma and comparison with neoclassical theory

Weston M. Stacey[1] **and Brian A. Grierson**[2]

[1] Georgia Institute of Technology, Atlanta, GA 30332, USA
[2] Princeton Plasma Physics Laboratory, Princeton, NJ 08543, USA

Received 21 January 2014, revised 17 March 2014
Accepted for publication 8 April 2014
Published 8 May 2014

Abstract

A low-confinement mode discharge which optimizes the capability of the new main-ion charge-exchange-recombination spectroscopy system on DIII-D (Luxon 2002 *Nucl. Fusion* **42** 614) to measure deuterium toroidal velocity is interpretted in comparison with the predictions of neoclassical theory, with an emphasis on the plasma edge region. The observed peaking in the deuterium toroidal velocity near the separatrix is shown to be consistent with intrinsic co-rotation due to ion orbit loss. In general, the standard neoclassical toroidal and poloidal momentum transport rates are found to be smaller than those inferred from experiment.

Keywords: rotation, intrinsic rotation, momentum transport

(Some figures may appear in colour only in the online journal)

1. Introduction

Understanding rotation in tokamaks is important both for basic knowledge of momentum transport in tokamak plasmas and for the practical knowledge of effects of rotation on confinement and in stabilizing magnetohydrodynamic (MHD) instabilities. There is experimental evidence of the relationship between rotation and energy confinement (e.g. [1] and [2]) and theoretical evidence for the relation of rotation to particle pinches and diffusion coefficients (e.g. [3]). There are both theoretical (e.g. [4]) and experimental (e.g. [5]) evidence that MHD resistive wall modes are stabilized by rotation.

Measurement of the toroidal and poloidal rotation velocities of impurity ions (in particular carbon) by charge-exchange-recombination (CER) spectroscopy (e.g. [6]) has provided a widely available tool for the study of impurity ion rotation for a number of years, but until recently there has been no direct measurement of the main deuterium ion rotation, and there are reasons to believe the deuterium rotation might differ from the measured carbon rotation. However, recently the CER methodology has been extended [7, 8] on DIII-D [9] to enable experimental determination of deuterium toroidal rotation, providing an important new experimental capability for the investigation of rotation in tokamaks.

There also have been parallel theory and modelling applications [10–17] of neoclassical rotation theory to predict the measured toroidal carbon rotation and the previously unmeasured deuterium toroidal rotation, in DIII-D and elsewhere, over the past decade. For axisymmetric toroidal geometry, gyroviscosity is the leading neoclassical candidate. A version of extended neoclassical theory, based on a calculation of poloidal asymmetries in densities, flows, etc. in a 'circular' flux surface geometry [10, 12], was found to predict the order of magnitude (over-prediction by factors of 2–3,) of measured carbon toroidal velocities. However, a recent extension [15] of this methodology to an elongated flux surface geometry representation brought the agreement with carbon toroidal and poloidal rotation measurements to within 10–20%, except in the plasma edge.

Comparisons [16–19] of neoclassical poloidal velocity with experiment show mixed results. The NCLASS code [14] was found to systematically underpredict measured carbon rotation velocities [14], and similar results were found [13] using a slightly different theory that also included poloidal asymmetries. However, related theories, but extended to include heat flux terms in the viscosity and the $V_r \times B$ force, found somewhat better agreement with experiment [13], and neoclassical poloidal velocity calculations that include poloidal asymmetries and an elongated flux surface geometry representation [15] are in good agreement with experiment for two DIII-D H-mode discharges, except in the edge. Drift-kinetic calculations of probe flow measurements in DIII-D [18] are also showing reasonable agreement.

Now that the ability exists to measure toroidal rotation for the main deuterium ions as well as the primary impurity carbons ions, and an extended neoclassical theory which includes poloidal asymmetries and an elongated flux surface representation is available, it seems appropriate to undertake

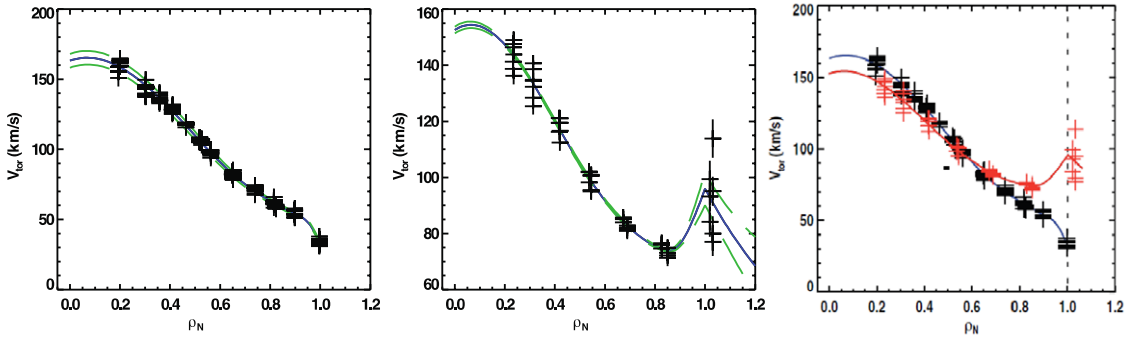

Figure 1. Toroidal velocity of (*a*) carbon, (*b*) deuterium and (*c*) both carbon and deuterium, fit with error bars from Monte-Carlo uncertainty error estimates. (ρ_N denotes the square root of the fraction of the enclosed toroidal flux, normalized to the value at the boundary.)

a new comparison of neoclassical rotation theory with experiment. On the theory comparison side, it seems logical to first sort out the various versions of neoclassical theory and separately compare them with experiment, in order to establish just what disagreement remains to be accounted for by turbulent and other transport mechanisms. Since there are more complicating factors in the edge—steep gradients, ion orbit loss, neutral recycling, strong structure in the rotation velocity and radial electric field profiles, etc—than in the core, this region requires special attention.

The purpose of this paper is to contribute to the comparison of neoclassical theory with rotation measurements now possible with the new CER experimental capability. A comparison of rotation measurements for both carbon and deuterium with the predictions of various versions of neoclassical theory is presented for a DIII-D discharge chosen to take advantage of the new experimental capability. We first present the rotation measurements and their comparison with the standard neoclassical analysis code NCLASS [14] in section 2, and then turn to a more detailed investigation of rotation in the tokamak plasma edge with theory. In section 3, the observed intrinsic co-rotation is compared with the prediction of ion-orbit-loss theory, and in section 4 the effects of ion orbit loss on the radial particle and energy fluxes transported outward in the plasma are calculated. In section 5, experimental toroidal angular momentum transport frequencies are interpreted from the measured toroidal rotation velocities and compared with predictions based on atomic physics and neoclassical momentum transfer mechanisms. In section 6, the measured poloidal carbon and inferred deuterium poloidal rotation velocities are compared with neoclassical predictions. Finally, we briefly discuss the extended neoclassical rotation methodology based on an elongated flux surface representation and taking into account poloidal asymmetries in particle and flow distributions [15], which would be expected to be important in plasmas with high flow rates and elongated divertor geometry.

2. Rotation measurements

The discharge chosen for the measurement and calculation of edge plasma rotational velocities is an L-mode plasma with heating from neutral beam injection (NBI). DIII-D discharge #149468 was designed specifically for rotation physics studies using the CER spectroscopy systems, whereby modulated NBI from both co-current and counter-current beams were used for toroidal rotation measurements of impurities and main-ions, and a third beam was used for carbon poloidal rotation measurements using vertically viewing CER sightlines [7, 8].

Some parameters for this discharge are plasma current and toroidal field of $I_p = 1.19$ MA and $B_t = -2.0$ T. Here the sign convention is positive current corresponds to the counter-clockwise direction when the tokamak is viewed from above (same direction as six of the eight NBI sources), and negative toroidal magnetic field is clockwise when viewed from above. In the right-handed coordinate system R, φ, Z, the plasma current direction defines the $+\varphi$ direction, and Z is the elevation. In the right-handed coordinate system of the plasma cross-section r, θ, φ, the + poloidal direction is down ($-Z$) on the outboard midplane. The + poloidal direction is also the direction of the poloidal field and the ion diamagnetic velocity direction.

This discharge positioned the plasma in the vacuum vessel with a large midplane gap between the equilibrium separatrix and the vessel wall. This plasma shape aligned the plasma edge with the outer-most sightlines of the main-ion CER (MI-CER) system and permitted a measurement of the deuterium toroidal velocity at the plasma edge. The L-mode edge makes the MI-CER measurements near the separatrix more feasible because the gradients are less steep than H-mode conditions and the measurement will suffer less from the spatial smearing which may occur near sharp changes in plasma profiles.

Presented in figure 1 are the profiles of carbon and deuterium toroidal velocity measured by the impurity (CER) and main-ion (MI-CER) CER systems. Both profiles are centrally peaked in this discharge with dominant co-current NBI. Carbon toroidal rotation measurements display a smooth decrease in velocity towards the plasma edge to approximately 35 km s^{-1} at $\rho = 1.0$, however the deuterium measurements display a clear increase in the toroidal rotation at the plasma separatrix near 80–110 km s^{-1}. Although the spatial resolution is insufficient to resolve the width of the co-current rotation feature very near the separatrix, and there is significant scatter, it can still be seen that the toroidal velocity of deuterium is more co-current than for carbon by approximately 45–75 km s^{-1} near the separatrix. (There is a finite spot size for the optical system of about 2 cm, so the last 'point', which appears outside the separatrix, should be regarded as an average over this increment.) Similar observations have been made using plunging Mach probes and appear to be a robust feature at the plasma boundary [18].

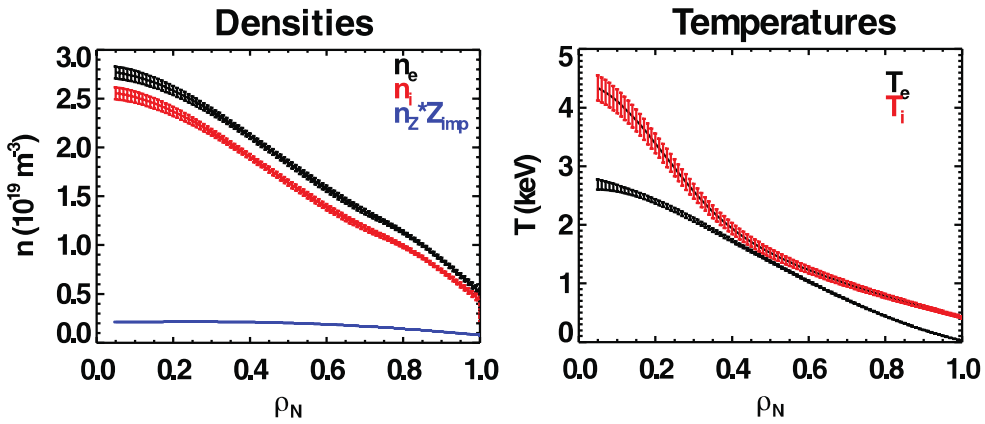

Figure 2. Profiles of (*a*) the electron density (upper) and deuterium (middle) and carbon (lower) ion densities and (*b*) electron (upper) and ion (lower) temperatures. (ρ_N denotes the square root of the fraction of the enclosed toroidal flux, normalized to the value at the boundary.)

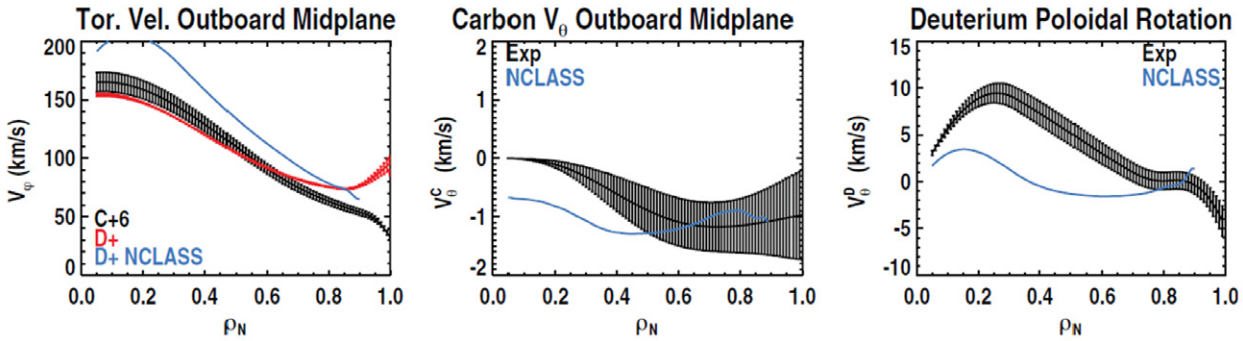

Figure 3. Toroidal velocity of carbon and deuterium (*a*), poloidal velocity of carbon (*b*) and poloidal velocity of deuterium (*c*). Overlayed are the predicted flow velocities from NCLASS (solid lines without error bars). (ρ_N denotes the enclosed fraction of the flux surface, or the 'normalized radius'.)

In order to assess the expected difference in the toroidal rotation of carbon and deuterium, we will use the radial force balance relation and calculations from neoclassical theory. Evaluation of the radial force balance relation and neoclassical calculations require the radial profiles of election and ion densities and temperatures, which are presented in figure 2. Electron density is measured by Thomson scattering and a multichannel CO_2 interferometer, carbon density is calculated from CER, and deuterium ion density is inferred from charge quasi-neutrality. Thomson scattering and ECE are used for electron temperature, and ion temperature is from CER. As described in [8] and [11], we can infer the deuterium ion poloidal velocity from the measured ion pressures, toroidal velocities (figure 3(*a*)), and the carbon poloidal velocity (figure 3(*b*)) arriving at a radially resolved main-ion poloidal flow (figure 3(*c*)).

Neoclassical theory from the NCLASS [14] model provides a calculation of the ion poloidal velocities of carbon and deuterium using the experimental equilibrium and profiles, and by using the ion radial force balance relation can therefore provide an expected deuterium ion toroidal velocity. Also displayed in figure 3 are the results of the NCLASS model using the experimental conditions. NCLASS predicts a larger toroidal flow for the main-ions than for carbon across the entire profile, but experimentally the main ion rotation is greater than the carbon ion rotation only at larger radii $\rho > 0.6$. The experimental carbon and deuterium poloidal flow velocities are more positive than NCLASS nearer the magnetic axis, but are of the same magnitude at larger radii. This result is consistent with previous observations [11] on DIII-D that (i) the poloidal flow is anomalous near steep gradients of the ion temperature and in the hot core where the collisionality is lower and (ii) that the flows are closer to NCLASS where the ion collisionality is higher at larger radii where the plasma is much cooler (figure 4), although the large error bars on the CER measurement of the carbon poloidal velocity are noted. The interfaces between the collisionality regimes are indicated by the dash line. We neglect to include the NCLASS evaluation for $\rho > 0.9$ because the evaluation of the flow velocities using the experimental loop voltage and neoclassical resistivity produces spurious results due to the large inductive parallel electric field term from $< E \times B >$.

3. Intrinsic co-rotation caused by ion orbit loss

An unique aspect of the measured rotation in the edge plasma is the strong peaking of the deuterium toroidal velocity at the separatrix, or co-current intrinsic rotation. There is rather strong recent evidence (e.g. [20–23] of intrinsic co-rotation in DIII-D and that it is produced by ion orbit loss [21–23] and not Reynold's stress [20]. We believe that the peaking in the measured deuterium toroidal rotation near the separatrix shown in figure 1(*b*) is an indication of intrinsic rotation, and we show in this section that ion orbit loss can produce this type of co-rotation peaking in the edge plasma rotation.

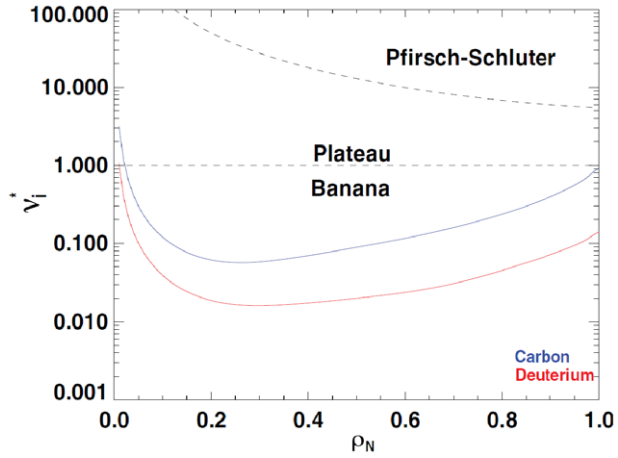

Figure 4. Normalized collision frequencies $\nu_j^* = \nu_{jk} q R / V_{\text{th}j}$ for carbon (upper curve) and deuterium (lower curve). (ρ_N denotes the enclosed fraction of the flux surface, or the 'normalized radius'.)

A calculation methodology has been developed [24–26] (based on the conservation of canonical angular momentum, energy and magnetic moment) which leads to an orbit constraint equation for the determination of the minimum speed for which an ion at some location on an internal flux surface, ψ_0, with initial speed V_0 and direction cosine ζ_0 with respect to the toroidal magnetic field can access a drift orbit which passes through some point on the separatrix ψ and be lost from the plasma

$$V_0^2\left[\left(\left|\frac{B}{B_0}\right|\frac{f_{\varphi 0}}{f_\varphi}\zeta_0\right)^2 - 1 + \left(1-\zeta_0^2\right)\left|\frac{B}{B_0}\right|\right] + V_0\left[\frac{2e\left(\psi_o-\psi\right)}{\text{Rmf}_\varphi}\left(\left|\frac{B}{B_0}\right|\frac{f_{\varphi 0}}{f_\varphi}\zeta_0\right)\right] + \left[\left(\frac{e\left(\psi_0-\psi\right)}{\text{Rmf}_\varphi}\right)^2 - \frac{2e\left(\phi_0-\phi\right)}{m}\right] = 0 \tag{1}$$

where $f_\varphi = |B_\varphi/B|$, R is the major radius, ϕ is the electrostatic potential and ψ is the flux surface value.

Equation (1) is quite general with respect to flux surface geometry representation of R, B and the flux surfaces ψ. By specifying an initial '0' location for an ion with initial direction cosine ζ_0, and specifying a final location on the flux surface ψ, equation (1) can be used to determine if an ion with speed $V_0(\zeta_0)$ can cross the separatrix at that final location on the flux surface ψ (i.e. if equation (1) has a physically reasonable solution).

Thus, equation (1) can be solved repeatedly to determine the minimum ion energy necessary for an ion located on an internal flux surface at many different points (ψ_0, θ_0) to cross the last closed flux surface at any location. All of the ions at this location (ψ_0, θ_0) with this value of ζ_0 and with speeds greater than this $V_{0\,\text{min}}(\psi_0, \zeta_0, \theta_0)$ are able to cross the last closed flux surface. Because ions move over the flux surface many times as they flow radially across it, the minimum value for any θ_0 is the minimum speed associated with the flux surface $V_{0\,\text{min}}(\psi_0, \zeta_0)$. We will assume in this work that a fraction $R_{\text{loss}}^{\text{iol}}$ of these ions crossing the last closed flux surface strike the chamber or divertor wall, interact with plasma or neutrals in the scrape-off layer, etc. such as not to return back across the last closed flux surface into the confined plasma.

For the usual DIII-D anti-parallel current/magnetic field configuration in shot #149468, the quantity $V_{0\,\text{min}}(\zeta_0)$ is very large for particles with parallel velocity components opposite to the direction of the toroidal magnetic field ($\zeta_0 < 0$), which execute banana orbits inside the flux surface, but becomes smaller with increasing $\zeta_0 > 0$ (i.e. as the particle velocity becomes more nearly aligned with the toroidal magnetic field direction). (Some detailed calculations for a DIII-D shot are discussed in [25] and [26]).

The GTEDGE code used to make the calculations discussed in this paper calculates $V_{0\,\text{min}}(\zeta_0)$ using the electrostatic potential calculated by integrating the (experimental or other) input radial electric field, an approximate 'circular' representation of the magnetic flux surface geometry described by $[R(r,\theta) = \overline{R}h(r,\theta)$, $B_{\theta,\varphi}(r,\theta) = \overline{B}_{\theta,\varphi}/h(r,\theta)$, $h(r,\theta) = (1 + (r/\overline{R})\cos\theta)]$, and an approximate flux surface representation $\psi(\rho) = RA_\varphi = \frac{1}{2}(\frac{\mu_0 I}{2\pi a^2})\overline{R}\overline{a}^2\rho^2$ which follows from Ampere's law and the assumption of uniform current density. Experimental data used in the calculation are mapped from the ρ_N(normalized enclosed magnetic flux) of the EFIT flux surface calculated for the experiment to the corresponding normalized radius of the circular model, and the geometric radii of the circular flux surfaces are constructed to conserve the corresponding experimental flux surface areas.

In the 'standard' DIII-D anti-parallel current/toroidal field configuration (the configuration of shot #149468) the preferential loss of $\zeta_0 > 0$ (counter-current) ions causes a residual $\zeta_0 < 0$ (co-current) intrinsic rotation in the edge plasma due to the preferential retention of co-current direction ions. The net co-current rotation velocity at any flux surface is determined by the cumulative net counter-current directed ion orbit loss that has taken place in the outflowing plasma at all inner radii out to that flux surface in question. Determining the minimum loss speed $V_{\text{min}(\zeta_0)}$ as described above allows writing an expression for the equivalent net parallel counter-current momentum loss rate (or co-current momentum gain rate) due to ion orbit loss $\Delta M_{\phi j}^{\text{iol}} = |B_\phi/B| nm\nu_{dj}\Delta V_\parallel$ (ν_{dj} is the toroidal momentum transport frequency discussed in section 6), which can be used to compute the intrinsic co-rotation caused by ion orbit loss, where [25, 26]

$$\begin{aligned}\Delta V_\parallel(\rho) &= R_{\text{loss}}^{\text{iol}} 2\pi \int_{-1}^{1} \text{d}\zeta_0 \left[\int_{V_{\text{min}}(\zeta_0)}^{\infty} (V_0\zeta_0)\, V_0^2 f(V_0)\text{d}V_0\right]_\rho \\ &= 4\pi M_{\text{orb}}(\rho)\left[\int_0^\infty (V_0)\, V_0^2 f(V_0)\text{d}V_0\right]_\rho \\ &= 2\frac{\Gamma(2)}{\pi^{1/2}} M_{\text{orb}}(\rho)\, V_{\text{th}}(\rho) = \frac{2}{\pi^{1/2}} M_{\text{orb}}(\rho)\sqrt{\frac{2kT_{\text{ion}}(\rho)}{m}}\end{aligned} \tag{2}$$

and an initially Maxwellian distribution of ions flowing outward through the edge has been assumed, to obtain

$$\begin{aligned}M_{\text{orb}} \equiv \frac{M_{\text{loss}}}{M_{\text{tot}}} &= \frac{R_{\text{loss}}^{\text{iol}}\int_{-1}^{1}\left[\int_{V_{0\,\text{min}}(\zeta_0)}^{\infty}(mV_0\zeta_0)\, V_0^2 f(V_0)\text{d}V_0\right]\text{d}\zeta_0}{2\int_0^\infty (mV_0)\, V_0^2 f(V_0)\text{d}V_0} \\ &= \frac{R_{\text{loss}}^{\text{iol}}\int_{-1}^{1}\zeta_0\Gamma\left(2, \varepsilon_{\text{min}(\zeta_0)}\right)\text{d}\zeta_0}{2\Gamma(2)}\end{aligned} \tag{3}$$

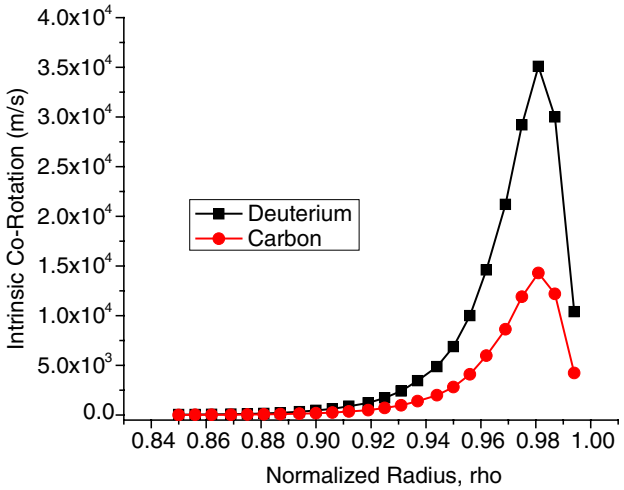

Figure 5. Calculated intrinsic co-rotation of carbon and deuterium ions produced by ion orbit loss for discharge 149 468 (loss fraction $R^{\rm iol}_{\rm loss} = 1.0$). ($\rho$ denotes the enclosed fraction of the magnetic flux, or the 'normalized radius'.)

$\Gamma(n, x)$ is the incomplete gamma function, and $\Gamma(n)$ is the gamma function. The reduced energy $\varepsilon_{\rm min}(\zeta_0) \equiv mV^2_{0\,\rm min}(\zeta_0)/2kT$ has been defined. When the current and toroidal field are anti-parallel, this net counter-current momentum loss (reduction) rate produces an intrinsic co-current rotation given by equation (2). Although ion species with the same charge-to-mass ratio Ze/m (e.g. deuterium and carbon) will have the same $V_{\rm min}(\zeta_0)$, the intrinsic rotation will decrease with ion mass both because $M_{\rm orb}$ (because the minimum energy corresponding to the minimum loss speed scales with ion mass) and because the thermal velocity decreases with ion mass, for the same ion temperature, with the result that ion orbit loss and intrinsic rotation are significantly stronger for deuterium than carbon ions.

This methodology was applied to DIII-D discharge 149 468 to calculate the intrinsic co-rotation profiles of ion orbit loss of thermal deuterium and carbon ions, and the resulting co-rotation is shown in figure 5. As the radius increases near the edge the cumulative loss of counter-rotating ions from the outward flowing plasma increases, leaving a plasma with a cumulatively increasing net co-rotation. However, sufficiently close to the separatrix, most of the counter-direction ions have been lost and it becomes possible for co-rotating ions to be lost, thus reducing the cumulative net co-rotation of the remaining ions in the outward flowing plasma and resulting in a peak in the intrinsic co-rotation just inside the separatrix. The intrinsic co-rotation shown in figure 5 is very similar in magnitude to the experimental co-rotation peaking (above the extrapolated core rotation profiles) for deuterium shown in figure 1. We note that a similar phenomenon has been observed in DIII-D probe measurements of the deuterium velocity in the edge plasma [18]. The experimental uncertainty in the location of the separatrix probably accounts for the somewhat more outward location of the peak in figure 1 than in figure 5.

The intrinsic rotation calculated from equation (2) and plotted in figure 5 is a flux-surface averaged value [25, 26] for the purpose of comparison with the experimental measurement shown in figure 1. However, the intrinsic rotation produced by ion orbit loss is poloidally asymmetric [26].

We note that the ion orbit loss calculation discussed above and used previously to interpret probe measurement of intrinsic deuterium rotation in DIII-D [23] is based on the same set of conservation equations [24] as the similar model by deGrassie [20–22] used to interpret probe measurements of intrinsic rotation in a different DIII-D discharge [18], although the computational implementation differs. In the model used in this paper the outward flowing plasma encounters a larger 'loss cone' at successive radii and the differential loss cone at any radius is replenished primarily by plasma flow from inner radii, not by in-scattering, which would increase the calculated loss. From figure 4, we would expect the rate at which ions are scattered into the differentially increased loss region at any radius to be small compared to the rate at which they are flowing in from smaller radii. This neglect of additional loss by scattering is compensated by the assumption that all ions which cross the separatrix are lost (i.e. $R^{\rm iol}_{\rm loss} = 1.0$) and none re-enter the plasma; refinements to these two aspects of the ion orbit loss calculation are being developed.

4. Radial ion flux

The radial ion flux appears as a $V \times B$ force in the toroidal and poloidal momentum balance equations, hence in the theoretical expressions for the rotation velocities. Integration of the steady-state particle continuity equation for species 'j'

$$\nabla \cdot n_j V_j \equiv \nabla \cdot \Gamma_j = S_{nbj} + n_{0j} n_{\rm e} \langle \sigma_{\rm ion} \upsilon \rangle_j \equiv S_{nbj} + n_{\rm e} \nu_{{\rm ion}\,j} \equiv S_j \quad (4)$$

determines the flux-surface averaged radial component of the ion particle flux, which is denoted Γ_{rj} and is usually outward. The first term on the right is the neutral beam or pellet particle source rate of ions of species 'j' and the second term is the ion particle source rate due to ionization of recycling or fuelling neutral atoms of species 'j'. A similar equation is obtained for all ion species present in the plasma, in particular for the main ion and impurity species with which we will be concerned in this paper.

A cumulative (with radius) fraction $F_{{\rm orb}\,j}(r)$ of this total particle flux Γ_{rj} resulting from external sources is lost from the edge region across the separatrix by ion-orbit-loss and by gradB drifting outward through the X-region (X-loss) [27, 28] of the thermalized plasma ions and the fast beam ions, thereby reducing the actual flux of particles being transported radially outward from the value calculated from equation (4) to $_{rj} \equiv (1 - F_{{\rm orb}\,j})\Gamma\widehat{\Gamma}_{rj}$. The quantity $F_{{\rm orb}\,j}(r)$ is calculated by a formula similar to equation (3) but without the $(mV_0\zeta_0)$ term in the integrands and with the arguments of the gamma functions $n = 3/2$.

In order to maintain charge neutrality, the loss of both thermalized plasma ions and fast beam ions by ion-orbit-loss and X-loss must be compensated by an inward current. Since the electrons are generally more effectively tied to field lines than are the ions, this current must be primarily carried by the ions [29]. The ion orbit loss is assumed to be balanced by an inward return current with a divergence at each radius that offsets the ion orbit loss, and this current is included in the calculation of the net radial particle flux flowing

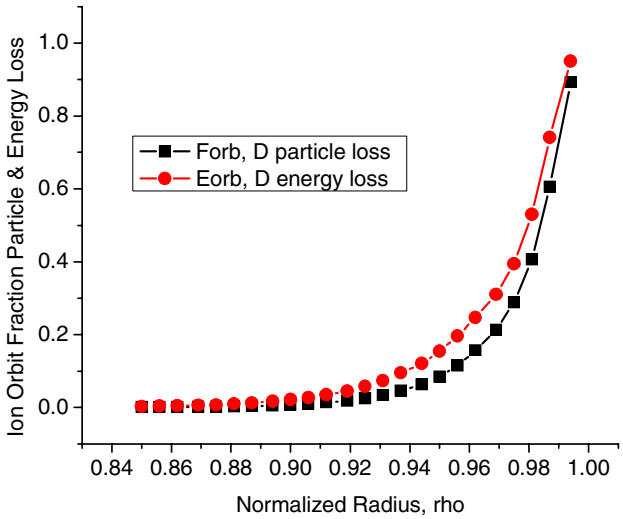

Figure 6. Ion orbit loss fractions for particles and energy for discharge 149 468 (fraction of ions crossing sepatrix which are lost $R^{\rm iol}_{\rm loss} = 1.0$). ($\rho$ denotes the enclosed fraction of the magnetic flux, or the 'normalized radius'.)

in the plasma. This total inward current must compensate the ion-orbit-loss from both the 'thermalized' plasma ions (main ion and impurities) and the fast neutral beam ions, $j_r = j_r^{\rm iol} + j_r^{\rm nbi}$. (In this paper we neglect the beam ion loss contribution to this current). Because the ion orbit loss for the main (deuterium) ion species 'j' is much greater than for the impurity (carbon) ion species 'k', we make the approximation $j_r^{\rm iol}(r) = -e_j F_{{\rm orb}j}\Gamma_{rj} - e_k F_{{\rm orb}k}\Gamma_{rk} \simeq -e_j F_{{\rm orb}j}(r)\Gamma_{rj}(r)$. In this paper we will be concerned with the ion orbit loss of thermalized plasma ions, which we consider to be likely to affect the edge plasma structure, but note that in general the loss of fast neutral beam ions should also be taken into account.

Assuming that the inward compensating current is carried by the main ion species, the net outward particle flux of the main ion species in the plasma due to loss of 'thermalized' plasma ions (taking into account ion-orbit-loss and any X-loss of outward flowing ions and the compensating inward current of main ions from the scrape-off layer) is then $\widehat{\Gamma}_{rj} \simeq (1 - F_{{\rm orb}j})\Gamma_{rj} - F_{{\rm orb}j}\Gamma_{rj} = (1 - 2F_{{\rm orb}j})\Gamma_{rj}$, where again Γ_{rj} would be the outward main ion flux due to the neutral beam and recycling neutral sources in the absence of any ion-orbit-loss or X-loss of ions or compensating inward current. A negative value of $\widehat{\Gamma}_{rj}$, as will occur in the edge when $F_{{\rm orb}j} > 0.5$, indicates a net inward flux of the main ions flowing in the plasma. Since it is assumed that the compensating return current is carried by ions of the main species 'j' and that ion orbit loss of the impurity species 'k' is negligible, the ion orbit loss can be taken into account by replacing Γ_{rj} with $\widehat{\Gamma}_{rj} \equiv (1 - 2F_{{\rm orb}j})\Gamma_{rj}$ for the main ions, but using the value of Γ_{rk} calculated from the continuity equation for the impurity ion species.

The values of the $F_{{\rm orb}j}(r)$ ion particle loss fraction and a similar ion energy loss fraction $E_{{\rm orb}j}(r)$ (calculated from equation (3), but with the $(mV_0\zeta_0)$ term in the integrands replaced by $(1/2mV_0^2)$ and with the arguments of the gamma functions changed to $n = 5/2$) are shown in figure 6. These calculations indicate that most of the deuterium particle and energy fluxes in the very edge is due to ion orbit loss.

While Γ_{rj} is calculated [25] for the main deuterium ions by integrating the continuity equation with neutral beam and recycling neutral ionization sources, in the absence of a multi-charge state model for calculating the carbon influx, we treat carbon as a single impurity species with a density which is a constant fraction of the deuterium density and that has the same density and temperature gradient scale lengths as deuterium, and calculate an average charge state which varies with radius from a fit to a coronal equilibrium calculation. For the equilibrium condition of this discharge at 1900 ms, the absence of an internal carbon source in the plasma implies $\Gamma_{rk} \approx 0$ in the plasma edge.

5. Ion toroidal rotation velocities

The continuity equation (4) can be combined with the momentum balance equation to obtain a balance among the inertial, pressure, viscous, electric field, $V \times B$, collisional friction and external source force terms [30]

$$n_j m_j \left(\boldsymbol{V}_j \cdot \nabla\right)\boldsymbol{V}_j + \nabla p_j + \nabla \cdot \Pi_j = n_j e_j \left(\mathrm{E} + \boldsymbol{V}_j \times \boldsymbol{B}\right) + \boldsymbol{R}_j^1 + \left(\boldsymbol{S}_j^1 - m_j \boldsymbol{V}_j S_j\right) \quad (5)$$

where R_j^1 and S_j^1 are the first velocity moments of the collision operator and the particle source.

Neglecting ion orbit loss effects for the moment, in a two-ion-species plasma ('j' and 'k'), the toroidal component of the momentum balance equation for species 'j' can be written

$$B_\theta e_j \Gamma_{rj} = n_j m_j (\nu_{dj} + \nu_{jk}) V_{\phi j} - n_j m_j \nu_{jk} V_{\phi k} - (M_{\phi j} + n_j e_j E_\phi^A) \quad (6)$$

and the equation for the other ion species 'k' is obtained by interchanging the 'j' and 'k' subscripts. (This formalism is readily generalized to multiple species by summing over 'k'.) The quantity $\nu_{dj} \equiv \nu^\phi_{{\rm visc}\,j} + \nu^\phi_{{\rm inert}\,j} + \nu^\phi_{{\rm anom}\,j} + \nu_{{\rm at}\,j}$ is a composite toroidal momentum exchange frequency due to toroidal viscosity, toroidal inertia (Reynold's stress), 'anomalous' viscosity (e.g. due to turbulence, non-axisymmetric toroidal magnetic field, etc.), respectively, and $\nu_{{\rm at}\,j} = \nu_{{\rm ion}\,j} + \nu_{{\rm elcx}\,j}$ is an atomic physics momentum exchange term involving ionization, elastic scattering and charge-exchange. The quantity $\nu_{dj} + \nu_{jk}$ represents the total toroidal momentum exchange, or 'transport', frequency for ions of species 'j' by transport processes and by momentum exchange with other ion and neutral species present in the plasma edge. Justification for writing the viscous and inertial momentum transfer in this form is discussed in [31] and [15]. $M_{\phi j} = M^{\rm nbi}_{\phi j} + \Delta M^{\rm iol}_{\phi j} + M^{\rm anom}_{\phi j}$ is the toroidal momentum input from neutral beams (calculated), from ion orbit loss ($\Delta M^{\rm iol}_{\phi j} = |B_\phi/B| n_j m_j \nu_{dj} \Delta V_{\|j}$) and from other sources (e.g. E_ϕ^A is the induced toroidal electric field (measured)), and the other quantities have their universally understood meaning.

Equation (6) and the corresponding equation for species 'k' can be solved for the unknown viscous + inertial + atomic + anomalous toroidal momentum transport frequency (ion orbit loss terms are now included)

$$\nu^{\rm exp}_{dj} = \frac{1}{(V^{\rm meas}_{\phi j} - \Delta V^{\rm iol}_{\phi j})}\left[\frac{B_\theta e_j \Gamma_{rj}\,(1 - 2F_{\rm orb})}{n_j m_j} + \nu_{jk}(V^{\rm meas}_{\phi k} - V^{\rm meas}_{\phi j}) + \frac{(M^{\rm nb}_{\phi j} + \Delta M^{\rm iol}_{\phi j}) + n_j e_j E^{\rm A}_\phi}{n_j m_j}\right] \quad (7)$$

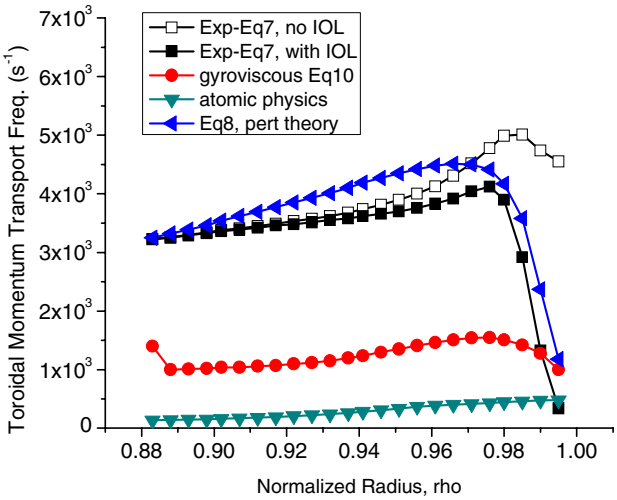

Figure 7. Deuterium toroidal momentum transport frequency ν_{dj} (IOL Loss fraction $R^{\rm iol}_{\rm loss} = 0.5$). ($\rho$ denotes the enclosed fraction of the magnetic flux, or the 'normalized radius'.)

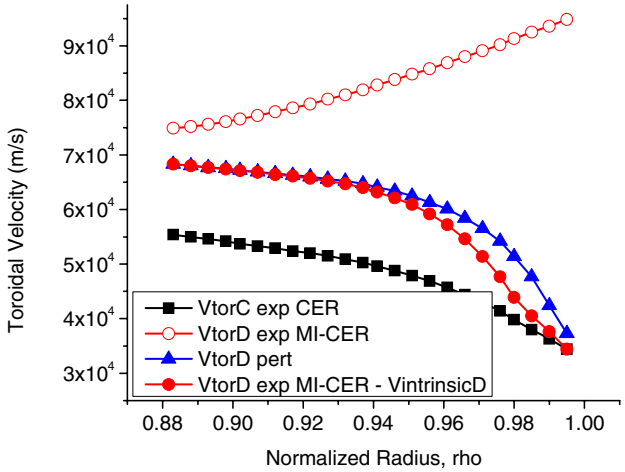

Figure 8. Comparison of measured and perturbation estimates of deuterium toroidal velocity. (Measured VtorD is shown by empty circles and with intrinsic rotation subtracted by solid circles. Measured carbon rotation is shown by solid squares, and the perturbation theory estimate of VtorD obtained by adding equation (9) to the carbon measurements is shown by solid triangles.) (IOL Loss fraction $R^{\rm iol}_{\rm loss} = 0.5$). ($\rho$ denotes the enclosed fraction of the magnetic flux, or the 'normalized radius'.)

where $\Delta V^{\rm iol}_{\phi j}$ is the toroidal component of the intrinsic rotation, and there is a similar equation for $\nu^{\rm exp}_{dk}$ with the subscripts 'j' and 'k' interchanged. Flux surface averaged quantities are implied in equation (7). Thus, the magnitude and profile of the momentum transport frequencies that are required to produce the measured toroidal rotation velocities can be determined and compared with the predictions of various theories. A plot of equation (7), evaluated using the data given in section 2, is shown by the solid squares in figure 7, and a plot of the same equation with the ion orbit loss terms $((F_{\rm orb}, \Delta V^{\rm iol}_{\phi j}, \Delta M^{\rm iol}_{\phi j})$ suppressed is shown by the empty squares. Taking ion orbit loss into account clearly affects the determination of the experimental toroidal momentum transport frequency in the edge region.

Also shown in figure 7 are the toroidal momentum transport frequencies (i) estimated from a perturbation theory that can be used in the absence of deuterium velocity measurements, (ii) calculated from neoclassical gyroviscosity and (iii) due to atomic physics processes (charge-exchange and ionization). The perturbation theory and the neoclassical gyroviscosity are briefly summarized below.

As mentioned, the ability to measure the deuterium velocity is relatively newly developed and not widely available. A perturbation theory procedure has been developed [32] for estimating reasonable values of the ν_{dj} and the 'experimental' velocity for deuterium using only the measured carbon toroidal velocity. The new capability to measure the deuterium toroidal velocity provides an opportunity to test this perturbation procedure, which is derived by first assuming a common toroidal momentum transport frequency $\nu^{\rm pert}_{d0} = \nu_{dj} = \nu_{dk}$ and summing the toroidal momentum balance equations (6) for the two ion species to obtain

$$\nu^{\rm pert}_{d0} = \frac{\left[\{\}_j + \{\}_k\right]}{\left[n_j m_j \left(V_{\phi k} + \Delta V_\phi\right) + n_k m_k V_{\phi k}\right]} \qquad (8)$$

where $\{\}_j \equiv \left\{B_\theta e_j \Gamma_{rj} + M_{\phi j} + n_j e_j E^{\rm A}_\phi\right\}$. An equation for the quantity $\Delta V_\phi \equiv V_{\phi j} - V_{\phi k}$ can be determined by subtracting the two toroidal momentum balance equations (6)

$$\Delta V_\phi = \left[\left(1 - \frac{\nu_{kj}}{\left(\nu_{kj} + \nu_{dk}\right)}\right) \frac{\{\}_j}{n_j m_j \left(\nu_{jk} + \nu_{dj}\right)} - \left(1 - \frac{\nu_{jk}}{\left(\nu_{jk} + \nu_{dj}\right)}\right) \frac{\{\}_k}{n_j m_j \left(\nu_{kj} + \nu_{dk}\right)}\right] \times \left[1 - \frac{\nu_{jk}\nu_{kj}}{\left(\nu_{jk} + \nu_{dj}\right)\left(\nu_{kj} + \nu_{dk}\right)}\right]^{-1} \qquad (9)$$

A surrogate for the experimental deuterium toroidal velocity $V^{\rm `exp'}_{\phi j} = V^{\rm meas}_{\phi k} + \Delta V_{\phi 0}$ can then be constructed from the measured value of the carbon velocity $V^{\rm meas}_{\phi k}$ and equation (9) by using $\nu_{dj} = \nu_{dk} = \nu_{d0}$ given by equation (8). We improve the solution of the nonlinear set of equations (8) and (9) iteratively, and find that the process converges when $|\Delta V_{\phi 0}/V^{\rm `exp'}_{\phi k}| \ll 1$. The converged perturbation calculation for $\nu_{dj} \simeq \nu_{d0}$. This perturbation interpretation using only the measured carbon velocity, shown with solid leftward-pointing triangles in figure 7, clearly agrees closely with the interpretation of the experimental toroidal momentum transport rate of equation (7) using both the measured carbon and deuterium toroidal velocities.

The measured carbon toroidal velocity (VtorC) and the perturbation estimate of the deuterium toroidal velocity (VtorD) constructed from it using equations (8) and (9) are compared with the measured deuterium VtorD, with and without the intrinsic deuterium rotation of figure 5 being subtracted, in figures 7 and 8 This result indicates that the intrinsic rotation is a large fraction of the total measured toroidal rotation for deuterium in the edge and that the perturbation estimate of the deuterium toroidal velocity is quite accurate when the experimental result is corrected for the intrinsic rotation of deuterium. Judging from figure 1, further taking into account the effect of the smaller intrinsic rotation of carbon would not greatly affect the agreement of the

perturbation estimate with the measured value. Alternatively, instead of correcting the result of the perturbation calculation for the intrinsic velocities due to ion orbit loss, the contributions of ion orbit loss to the momentum input, $\Delta M^{\rm iol}_{\phi j,k}$, could be included in the $\{\}_{j,k}$ terms in equations (8) and (9).

With respect to comparison with neoclassical toroidal rotation theory, Braginskii's strong rotation decomposition of the flow rate-of-strain tensor [33] has been generalized [34] to toroidal 'circular' flux surface $(1+\varepsilon\cos\theta)$ geometry and more recently [15] to elongated 'Miller model' flux surface geometry, and extended to include a neoclassical parallel viscosity coefficient [35]. Because the flux surface average of the toroidal component of the divergence of the parallel viscosity tensor vanishes identically in axisymmetric geometry and because the perpendicular viscosity coefficient is orders of magnitude too small (even with neoclassical corrections), the gyroviscosity is the relevant neoclassical toroidal viscosity in toroidally axisymmetric systems.

We plan to make a comparison of the elongated flux surface gyroviscosity calculation [15] over the full plasma radius with measurements of the deuterium toroidal velocities over the coming year, and this will be reported in a future paper. For now, the gyroviscous momentum transport frequency is calculated using the circular flux surface geometry model and expanding the poloidal dependences in a first-order Fourier series to obtain a set of equations to be solved for the sin and cos components of the poloidal asymmetries in flows, densities and electrostatic potential (the quantities with the sine (s) and cosine (c) superscripts in equation (10)) and finally to evaluate the flux surface average of the divergence of the gyroviscosity tensor to obtain an expression for the toroidal momentum transport frequency [15], which is plotted as solid circles in figure 7.

$$\nu^{\rm gyro}_{dj} = \frac{1}{2}G\Theta\frac{T_j}{e_j B_\phi R^2},\ G = r\left(L_n^{-1}+L_T^{-1}+L_{V_\phi}^{-1}\right),$$
$$L_X^{-1} = \frac{-1}{X}\frac{\partial X}{\partial r}$$
$$\Theta = \left[4+\left(\frac{n^{\rm c}}{\varepsilon}\right)\right]\left(\frac{V_\phi^{\rm s}}{\varepsilon}\right)+\left[1-\left(\frac{V_\phi^{\rm c}}{\varepsilon}\right)\right]\left(\frac{n^{\rm s}}{\varepsilon}\right)$$
$$= \left[4+\left(\frac{n^{\rm c}}{\varepsilon}\right)\right]\left\{-\left(\frac{B_\phi}{B_\theta}\frac{V_\theta}{V_\phi}\right)\left[\left(\frac{\Phi^{\rm s}}{\varepsilon}\right)+\left(\frac{n^{\rm s}}{\varepsilon}\right)\right]+\left(\frac{\Phi^{\rm s}}{\varepsilon}\right)\right\}$$
$$+\left(\frac{n^{\rm s}}{\varepsilon}\right)\left\{\left(\frac{B_\phi}{B_\theta}\frac{V_\theta}{V_\phi}\right)\left[2+\left(\frac{\Phi^{\rm c}}{\varepsilon}\right)+\left(\frac{n^{\rm c}}{\varepsilon}\right)\right]-\left(\frac{\Phi^{\rm c}}{\varepsilon}\right)\right\}. \quad (10)$$

It is clear from the last of equation (10) that the gyroviscous momentum transport frequency depends on the poloidal asymmetries in flow, density and electrostatic potential over the flux surface, and in particular on the existence of up-down sine asymmetries. These asymmetries were calculated using the experimental rotation velocities as input to evaluate the gyroviscous terms in figure 7. The calculation model used for the evaluation of the asymmetries is known as the Stacey–Sigmar 'circular' model because of the circular flux surface representation and is described in [13, 15] and elsewhere.

Past comparisons with measurements of carbon toroidal rotation velocities in DIII-D have shown that the circular flux surface gyroviscosity representation over-predicted the experimental toroidal velocities [12] (under-predicted ν_{dj}) by a factor of 2–3, but that the elongated flux surface geometry model [15] predicted toroidal carbon velocities within 10–20% of the measured values except in the very edge where there was a larger disagreement for one of the two discharges evaluated. The predicted gyroviscosity frequency for deuterium shown in figure 6 is about a factor of 3 below the experimentally inferred value of the toroidal momentum transport frequency, so based on this previous experience [15] of a factor of 2–3 larger frequencies with an elongated flux surface model we would expect that gyroviscosity might be the proper magnitude to account for the toroidal momentum transport. We intend to carry out this calculation in elongated flux surface geometry [15] in the coming year.

6. Ion poloidal rotation velocities

The 'experimental' value of the deuterium poloidal velocity discussed in section 2 is constructed using the radial component of the momentum balance equation (5) for deuterium

$$V^{\exp'}_{\theta j} = \frac{1}{B_\phi}\left[B_\theta V^{\exp'}_{\phi j} - E_r^{\rm exp} + \frac{1}{n_j^{\rm exp}e_j}\frac{\partial p_j^{\rm exp}}{\partial r}\right] \quad (11)$$

and by using the radial component of the carbon momentum balance to evaluate the radial electric field

$$E_r^{\rm exp} = B_\theta V_{\phi k}^{\rm exp} - B_\phi V_{\theta k}^{\rm exp} + \frac{1}{n_k^{\rm exp}e_k}\frac{\partial p_k^{\rm exp}}{\partial r} \quad (12)$$

to obtain

$$V_{\theta j}^{\rm exp} = V_{\theta k}^{\rm exp} - \frac{T_k}{B_\phi}\left(L_{pj}^{-1}-\frac{1}{z_k}L_{pk}^{-1}\right)+\frac{B_\theta}{B_\phi}\left(V_{\phi j}^{\rm exp}-V_{\phi k}^{\rm exp}\right) \quad (13)$$

The value of the poloidal velocity for deuterium shown in figure 3(*c*) was obtained by using (i) CER measurements of the C6+ carbon density, temperature and rotation velocities, (ii) MI-CER measurements of the deuterium toroidal rotation, (iii) Thomson scattering measurements of electron density and temperature and (iv) the charge neutrality requirement to evaluate equation (13). This value of the rotation velocity (plotted again in figure 9 with solid square symbols and the label 'exp, MI-CER meas') is based on the implicit assumption that the total carbon density is the measured C + 6 density.

In the theoretical developments of this paper, the local carbon density is assumed to be a constant fraction (determined by CER measurement in a location where carbon is 100% C+6) of the deuterium density, which implies that all density gradient scale lengths are the same ($L_{nk}^{-1}\simeq L_{nj}^{-1}\simeq L_{ne}^{-1}$). The deuterium ion temperature T_j is assumed to be the same as the measured carbon temperature T_k. The result of equation (13), evaluated for ($L_{pk}^{-1}\simeq L_{pj}^{-1}\simeq L_{ne}^{-1}+L_{Tk}^{-1}$) and shown in figure 9 with solid triangles and labelled 'force balance equation (13)', is quite close to the 'experimental' result of the previous paragraph.

On the other hand, the result obtained by using the CER measurements to evaluate L_{pk}^{-1} in equation (12) and then using this value of $E_r^{\rm exp}$ together with $L_{pj}^{-1}\simeq L_{ne}^{-1}+L_{Tk}^{-1}$ in equation (11) to evaluate $V_{\theta j}^{\rm exp}$ resulted in a very different result shown in figure 9 by the solid circles and the label 'force

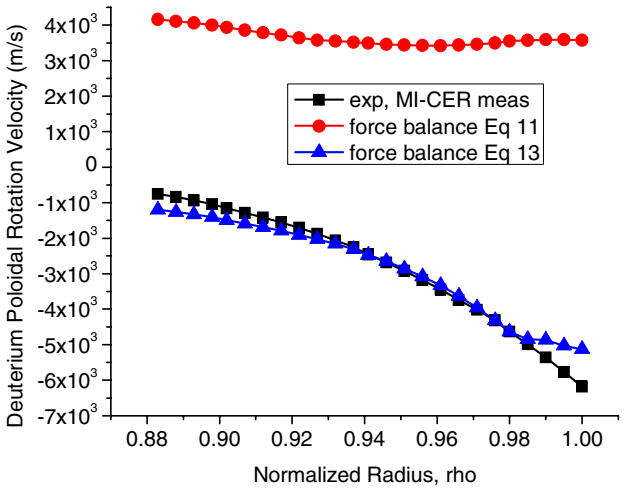

Figure 9. Comparison of different force balance determinations of the experimental deuterium poloidal rotation velocity. (ρ denotes the enclosed fraction of the magnetic flux, or the 'normalized radius'.)

balance equation (11)'. It seems that the inferred experimental deuterium poloidal velocity is relatively insensitive to which assumption is made about the relation of the measured C + 6 density to the total carbon density, so long as the same assumption is made everywhere in the calculation, but that the use of different assumptions (hence different evaluations of the pressure gradient scale lengths) in the same calculation can lead to the quite different results indicated by the solid circles in figure 9.

Theoretically, the poloidal rotation velocities for the two ion species are determined by the poloidal component of the momentum balance equations for each species. The poloidal momentum balance equation for ion species 'j' may be written [13]

$$\left(-\nu_{\mathrm{visc}\,j}+\nu_{jk}+\nu_{\mathrm{atom}\,j}\right)V_{\theta j}-\nu_{jk}V_{\theta k} = -B_\phi\left\{\frac{e_j}{n_j m_j}\Gamma_{rj}-\nu_{\mathrm{visc}\,j}\left(\frac{K^j T_j L_{Tj}^{-1}}{e_j B^2}\right)\right\} \tag{14}$$

The quantity $\nu_{\mathrm{visc}\,j}$ arises from the flux surface average of the poloidal components of the divergence of the viscosity tensor plus inertial (Reynold's stress) tensor plus other 'anomalous' mechanisms. In writing equation (14) terms involving poloidal asymmetries [12, 15] have been suppressed. A similar equation with the 'j' and 'k' sub/super-scripts interchanged obtains for the 'k' ion species.

With the two poloidal rotation velocities determined experimentally (carbon measured by CER, deuterium from radial force balance using CER and Thomson measurements), the two equations (14) can be solved for the poloidal momentum transport frequencies $\nu_{\mathrm{visc}\,j}$ and $\nu_{\mathrm{visc}k}$ as unknowns, using the experimental poloidal rotation velocities $V_{\theta j,k}^{\mathrm{meas}}$ as known inputs to obtain the experimental poloidal momentum transport frequencies that produce the measured poloidal rotation velocities

$$\nu_{\mathrm{visc}\,j}^{\mathrm{exp}} = \left[\frac{B_\phi \frac{e_j}{n_j m_j}\Gamma_{rj}\,(1-2F_{\mathrm{orb}})+\left(\nu_{jk}+\nu_{\mathrm{at}\,j}\right)V_{\theta j}^{\mathrm{exp}}-\nu_{jk}V_{\theta k}^{\mathrm{meas}}}{V_{\theta j}^{\mathrm{exp}}+\frac{B_\varphi K^j T_j}{e_j B^2}L_{Tj}^{-1}}\right] \tag{15}$$

and a similar equation with the 'j' and 'k' sub/super-scripts interchanged for $\nu_{\mathrm{visc}k}^{\mathrm{exp}}$. Again, for the main ion species 'j', the radial particle flux that enters the momentum balance is corrected for ion orbit loss to $\widehat{\Gamma}_{rj}=(1-2F_{\mathrm{orb}\,j})\Gamma_{rj}$, but for the impurity species 'k' $\widehat{\Gamma}_{rk}$ is replaced by $\widehat{\Gamma}_{rk}\equiv(1-F_{\mathrm{orb}k})\Gamma_{rk}$. (In the calculation presented in this paper we use $\Gamma_{rk}\simeq 0$.)

Alternatively, if poloidal momentum transport frequencies $\nu_{\mathrm{visc}k}$ are known from theory, then equation (14) for the two species may be solved for the poloidal rotation velocities

$$V_{\theta j}=-\frac{B_\phi}{\nu_{\theta j}}\frac{\left[\{\}_j+\frac{\nu_{jk}}{\nu_{\theta k}}\{\}_k\right]}{\left[1-\frac{\nu_{jk}\nu_{kj}}{\nu_{\theta j}\nu_{\theta k}}\right]} \tag{16}$$

where $\nu_{\theta j}=-\nu_{\mathrm{visc}\,j}+\nu_{jk}+\nu_{\mathrm{at}\,j}$ and now $\{\}_j=\left\{\frac{e_j\Gamma_{rj}(1-2F_{\mathrm{orb}\,j})}{n_j m_j}-\nu_{\mathrm{visc}\,j}\left(\frac{K^j T_j L_{Tj}^{-1}}{e_j B^2}\right)\right\}$. The expression $\{\}_k$ for impurity species 'k' does not have the factor of 2 because of the assumption that the return current is carried entirely by the main ion species.

Various theoretical poloidal momentum transport frequencies can be compared against the experimental values inferred from equation (15) or used to compute the poloidal rotation velocity with equation (16) for comparison with measured rotation velocities. For example, an extension [13] of the Hirshman–Sigmar [36] viscosity tensor (on which the NCLASS code [14] is based) results from retaining only the viscous and friction terms in the poloidal component of equation (5) and representing the parallel component of the viscous stress tensor as

$$\left\langle \boldsymbol{B}\cdot\nabla\cdot\Pi_j^{\parallel}\right\rangle^{HS}=-n_j m_j \nu_{jj}\left\langle B^2\right\rangle\frac{\mu_{00}^j}{B_\theta}\left(V_{\theta j}+\frac{B_\phi K^j T_j L_{Tj}^{-1}}{e_j B^2}\right) \tag{17}$$

Using the Lorentz form for the collisional friction and extending the original Hirshman–Sigmar theory to retain the $V_{\mathrm{r}}\times B$ term, we obtain the 'extended' Hirshman–Sigmar theory [13] for poloidal rotation in the form of equation (11) with $\nu_{\mathrm{visc}\,j}^{\mathrm{HS}}=\nu_{jj}\mu_{00}^j B/B_\theta$. Here

$$\begin{aligned}
\mu_{00} &= \frac{g\mu_{00}^{\mathrm{B}}}{\left(1.292\nu^*\mu_{00}^{\mathrm{B}}/\mu_{00}^{\mathrm{P}}\right)\left(1+\mu_{00}^{\mathrm{P}}\nu^*\varepsilon^{3/2}/6\mu_{00}^{\mathrm{PS}}\right)},\\
g &= \frac{\left(1.46\sqrt{\varepsilon}-0.46\varepsilon^{3/2}\right)}{\left(1-1.46\sqrt{\varepsilon}+0.46\varepsilon^{3/2}\right)},\\
\mu_{00}^{\mathrm{B}} &= 0.53+\alpha,\quad \mu_{00}^{\mathrm{P}}=3.54,\\
\mu_{00}^{\mathrm{PS}} &= (3.02+4.25\alpha)/\left(2.23+5.32\alpha+2.4\alpha^2\right),\\
\alpha &= n_k Z_k^2/n_j
\end{aligned} \tag{18}$$

The quantity $K^j=\mu_{01}^j/\mu_{00}^j$, where $\mu_{01}^j=2.5\mu_{00}^j-K_{01}$ and the K_{01} is interpolated like μ_{00} above but using instead $K_{01}^{\mathrm{B}}=0.71+\alpha$, $K_{01}^{\mathrm{P}}=10.63$ and $K_{01}^{\mathrm{PS}}=(12.43+20.13\alpha)/(2.23+5.32\alpha+2.4\alpha^2)$. The similar Kim–Diamond–Groebner (KDG) model [37] is a trace-impurity approximation to the Hirshman–Sigmar model.

Stacey and Sigmar *et al* [34, 35] generalized Braginskii's [33] flow rate-of-strain tensor in the strong rotation ordering to toroidal geometry and replaced the collisional Braginskii parallel viscosity coefficient with the Shaing–Sigmar

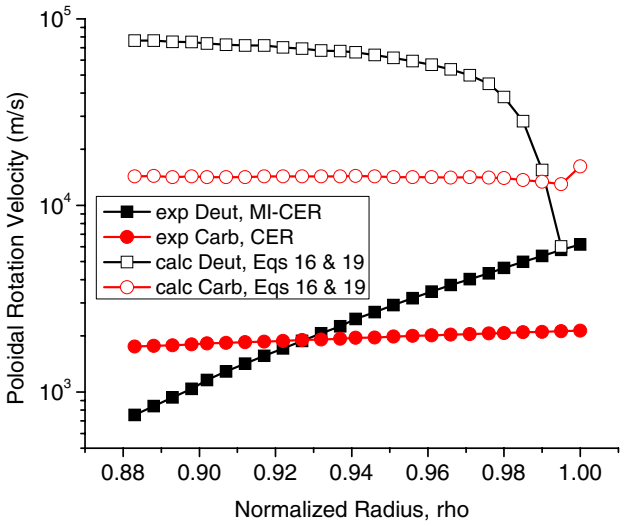

Figure 10. Comparison of neoclassical theory of equations (16) and (19) with measurements. (The sign of all velocities is in the negative sense in a $r-\theta-\varphi$ RHS with the toroidal direction in the direction of the plasma current.) (IOL loss fraction $R^{\rm iol}_{\rm loss}=0.5$). ($\rho$ denotes the enclosed fraction of the magnetic flux, or the 'normalized radius'.)

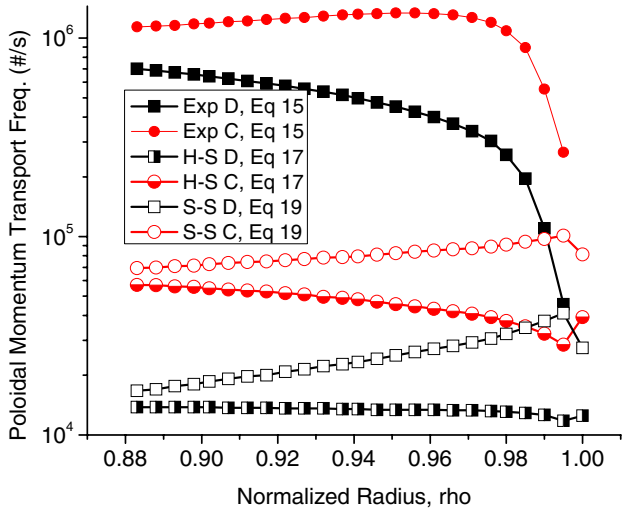

Figure 11. Comparison of experimental and theoretical deuterium poloidal momentum transport frequencies $\nu_{{\rm visc}\,j}$ (IOL loss fraction $R^{\rm iol}_{\rm loss}=0.5$). ($\rho$ denotes the enclosed fraction of the magnetic flux, or the 'normalized radius'.)

neoclassical coefficient [35] $\eta_{0j}=n_j m_j V_{{\rm th}\,j} q R f_j(\nu^*_{jj})$, $f_j\equiv \varepsilon^{-3/2}\nu^*_{jj}/(1+\varepsilon^{-3/2}\nu^*_{jj})(1+\nu^*_{jj})$, $\nu^*_{jj}\equiv \nu_{jj}qR/V_{{\rm th}\,j}$ to obtain

$$\left\langle \boldsymbol{B}\cdot\nabla\cdot\Pi^{\parallel}_j\right\rangle^{\rm SS}=-n_j m_j\frac{qV_{{\rm th}\,j}f_j\left(\nu_{jj}\right)}{R}\left(V_{\theta j}+\frac{B_\phi K^j T_j L^{-1}_{T_j}}{e_j B^2}\right) \tag{19}$$

They retained the viscous, friction and $V_{\rm r}\times B$ terms in the poloidal momentum balance to obtain an equation that reduces to equation (14) with $\nu^{\rm SS}_{{\rm visc}\,j}=qV_{{\rm th}\,j}f_j/R$ when poloidal asymmetries are suppressed. (A more general formalism is obtained when these poloidal asymmetries are retained [12, 15], and an even more general elongated flux surface geometry representation has recently been developed [15].)

The measured carbon and deuterium poloidal rotation velocities are compared against the neoclassical model of equations (16) and (19) in figure 10. The neoclassical theory significantly over-predicts the measured rotation velocities. A similar result was found when the neoclassical theory of equations (17) and (18) was used. A more detailed comparison of the theoretical predictions with experiment is given in [13].

Perhaps a more informative way to consider the difference in theory and experiment is in terms of the poloidal momentum transport frequencies inferred from measurements using equation (15) and calculated from theory as described above. As shown in figure 11, these neoclassical poloidal momentum transport rates are too small by an order of magnitude or more to account for the poloidal momentum transport rates inferred from experiment. We note that poloidal asymmetries have not been taken into account in evaluating the S-S poloidal momentum transport rates, and doing so would be expected to increase the S-S values [15].

At this point, we would have to conclude tentatively that the neoclassical poloidal momentum transport rate is too small by an order of magnitude to account for the measured poloidal rotation velocities, but that a definite conclusion must await calculations with the extended neoclassical theory [15] that takes into account poloidal asymmetries in an elongated flux surface geometry.

7. Summary

The extension of CER spectroscopy capability in DIII-D to measure the main deuterium ion toroidal velocity, as well as the carbon impurity ion toroidal and poloidal velocities, provides a valuable new tool for investigating rotation in tokamak plasmas. This paper describes the experimental results for an L-mode discharge positioned to take advantage of the new diagnostic capability. A preliminary comparison of the experimental results with neoclassical theory, in the form of a comparison with NCLASS [14] predictions of poloidal rotation and an in-depth analysis of toroidal and poloidal rotation in the plasma edge, was described.

One notable result was the identification of a peaking in the main deuterium ion toroidal co-rotation near the separatrix, confirming previous probe measurements. The magnitude of this rotation peaking was well-represented by the prediction of intrinsic co-current rotation caused by ion orbit loss.

NCLASS predictions of poloidal rotation were in reasonable agreement with measured values for $0.5<\rho<0.9$ for carbon and for $0.8<\rho<0.9$ for deuterium, but disagreed significantly for smaller radii. NCLASS does not predict toroidal velocity, but the NCLASS force balance prediction of the difference in deuterium and carbon toroidal velocities was of the wrong sign for $\rho<0.6$.

The edge region $\rho>0.9$ was investigated in some detail. A perturbation technique for estimating the deuterium toroidal velocity from the measured carbon velocity was shown to be quite accurate for this discharge by comparison with the measured deuterium toroidal velocity. Inferred experimental toroidal angular momentum transport rates were found to be about three times larger than the predicted gyroviscous transport rate (based on a circular flux surface representation)

and about an order of magnitude larger than atomic physics momentum transport rates.

The inferred poloidal momentum transport rates (viscous+ Reynold's stress + atomic physics) were an order of magnitude greater than the viscous poloidal momentum transport rates predicted by Hirshman–Sigmar [36], Stacey–Sigmar [35] and similar neoclassical parallel viscosity theories that neglect poloidal asymmetries, in the plasma edge.

Acknowledgments

The authors acknowledge their gratitude to other members of the DIII-D Team whose efforts have made these measurements possible, and in particular to Colin Chrystal for reducing the carbon spectroscopic data. The first author expresses his appreciation to General Atomics for their hospitality during part of this work. The work was supported by DOE grant DE-FG02-ER54538 with the Georgia Tech Research Corporation and by DOE contracts DE-AC02-09CH11466 with the Princeton Plasma Physics Laboratory and DE-AC03-99ER54463 with General Atomics.

References

[1] deGrassie J.S., Baker D.R., Burrell K.H., Gohil P., Greenfield C.M., Groebner R.J. and Thomas D.M. 2003 *Nucl. Fusion* **43** 142
[2] Rice J.E. *et al* 2012 *Phys. Plasmas* **19** 056106
[3] Stacey W.M., Groebner R.J. and Evans T.E. 2012 *Nucl. Fusion* **52** 114020
[4] Bondeson A. and Ward D.J. 1994 *Phys. Rev. Lett.* **72** 2709
[5] Garofalo A.M. *et al* 2001 *Nucl. Fusion* **41** 1171
[6] Gohil P., Burrell K.H. and Groebner R.J. 1992 *Proc. 14th Symp. on Fusion Engineering (San Diego, CA, 1991)* vol 2 (New York: IEEE) p 1199
[7] Grierson B.A., Burrell K.H., Chrystal C., Groebner R.J., Kaplan D.H., Heidbrink W.W., Munoz Burgos J.M., Pablant N.A., Solomon W.M. and Van Zeeland M.A. 2012 *Rev. Sci. Instrum.* **83** 10D529
[8] Grierson B.A., Burrell K.H., Heidbrink W.W., Lanctot M.J., Pablant N.A. and Solomon W.M. 2012 *Phys. Plasmas* **19** 056107
[9] Luxon J. 2002 *Nucl. Fusion* **42** 614
[10] Stacey W.M. and Mandrekas J. 2002 *Phys. Plasmas* **9** 1622
[11] Solomon W.M., Burrell K.H., Andre R., Baylor L.R., Budny R., Gohil P., Groebner R.J., Holcomb C.T., Houlberg W.A. and Wade M.R. 2006 *Phys. Plasmas* **13** 056116
[12] Stacey W.M., Johnson R.W. and Mandrekas J. 2006 *Phys. Plasmas* **13** 062508
[13] Stacey W.M. 2008 *Phys. Plasmas* **15** 012501
[14] Houlberg W.A., Shaing K.C., Hirshman S.P. and Zarnstorff M.C. 1997 *Phys. Plasmas* **4** 3230
[15] Bae C., Stacey W.M. and Solomon W.M. 2013 *Nucl. Fusion* **53** 043011
[16] Solomon W.M., Burrell K.H., Feder R., Nagy A., Gohil P. and Groebner R.J. 2008 *Rev. Sci. Instrum.* **79** 10F531
[17] Solomon W.M., Burrell K.H., Gohil P., Groebner R.J. and Baylor L. 2004 *Rev. Sci. Instrum.* **75** 3481
[18] Bodeo J.A. *et al* 2011 *Phys. Plasmas* **18** 032510
[19] Grierson B.A., Burrell K.H., Solomon W.M., Budny R.V. and Candy J. 2013 *Nucl. Fusion* **53** 063010
[20] deGrassie J.S., Groebner R.J., Burrell K.H. and Solomon W.M. 2009 *Nucl. Fusion* **49** 085020
[21] deGrassie J.S., Mueller S.H. and Bodeo J.A. 2012 *Nucl. Fusion* **52** 013010
[22] Mueller S.H., Boedo J.A., Burrell K.H., deGrassie J.S., Moyer R.A., Rudakov D.L., Solomon W.M. and Tynan G.R. 2011 *Phys. Plasmas* **18** 072504
[23] Stacey W.M., Boedo J.A., Evans T.E., Grierson B.A. and Groebner R.J. 2012 *Phys. Plasmas* **19** 112503
[24] Miyamoto K. 1996 *Nucl. Fusion* **36** 927
[25] Stacey W.M. 2011 *Phys. Plasmas* **18** 102504
[26] Stacey W.M. 2013 *Nucl. Fusion* **53** 063011
[27] Chang C.S., Kue S. and Weitzner H. 2002 *Phys. Plasmas* **9** 3884
[28] Stacey W.M. 2011 *Phys. Plasmas* **18** 122504
[29] McClements K.G. and Thyagaraja A. 2006 *Phys. Plasmas* **13** 042503
[30] Stacey W.M. 2012 *Fusion Plasma Physics* 2nd edn (Weinheim, Germany: Wiley-VCH) p 90
[31] Stacey W.M. 2008 *Contrib. Plasma Phys.* **48** 94
[32] Stacey W.M. and Groebner R.J. 2008 *Phys. Plasmas* **15** 012503
[33] Braginskii S.I. 1965 *Rev. Plasma Phys.* **1** 205
[34] Stacey W.M. and Sigmar D.J. 1985 *Phys. Fluids* **28** 2800
[35] Stacey W.M., Bailey A.W., Sigmar D.J. and Shaing K.C. 1985 *Nucl. Fusion* **25** 463
[36] Hirshman S.P. and Sigmar D.J. 1981 *Nucl. Fusion* **21** 1079
[37] Kim B., Diamond P.H. and Groebner R.J. 1991 *Phys. Fluids* B **3** 2050